

A library of human electrocorticographic data and analyses

Kai J. Miller^{1,2}

Electrophysiological data from implanted electrodes in the human brain are rare, and therefore scientific access to such data has remained somewhat exclusive. Here we present a freely available curated library of implanted electrocorticographic data and analyses for 16 behavioural experiments, with 204 individual datasets from 34 patients recorded with the same amplifiers and at the same settings. For each dataset, electrode positions were carefully registered to brain anatomy. A large set of fully annotated analysis scripts with which to interpret these data is embedded in the library alongside them. All data, anatomical locations and analysis files (MATLAB code) are provided in a shared file structure at <https://searchworks.stanford.edu/view/zk881ps0522>.

Clinical electrocorticography (ECoG) is the measurement of voltages from the human brain surface at the millimeter scale (Fig. 1). When compared with other techniques to examine human brain function, ECoG provides high spatial and temporal resolution, with the caveat that electrode placement is stochastic and sparse because of clinical considerations. However, by intrinsically averaging across a population, ECoG is not limited by stochastic responses to the same extent as single-unit measurements. Spatial resolution is high because the spatial scale of cortical columns is not much smaller than the exposed ECoG electrode surface^{1,2}. ECoG signal changes have been shown across a variety of brain regions and behavioural tasks to represent a robust general correlate of neuronal population activity³. Modelling and empirical data analysis suggest that broadband ECoG changes probably reflect changes in the average input firing rate to the neuronal population beneath each electrode^{4,5} (Fig. 2). This makes ECoG changes robust on a single-event scale (for example, faster than most individual perceptions, decisions and behaviours⁶), so the effect of immediate context may be examined on a single-trial basis with ~20 ms resolution^{7,8}, rather than average context across repeated events.

This library consists of experiments that were conducted on patients where medically indicated electrode placement coincided with regions known to induce functional magnetic resonance imaging blood-oxygen-level-dependent (fMRI BOLD) changes in specific experimental tasks. For each experiment, at least four patients shared the same brain region coverage and performed the same task. The accompanying MATLAB script library is tailored specifically to allow the identification and extraction of high-yield features from the ECoG signal (Figs. 2–4).

Results

This library of 16 experiments composed of 204 datasets is available for use without restriction at <https://searchworks.stanford.edu/view/zk881ps0522>.

Experimental setting. These ECoG data were recorded at the bedside during a monitoring period to localize seizure focus (the location in the brain where abnormal activity begins and from which it spreads) in patients with epilepsy at Harborview Hospital,

Seattle, WA, USA over a 7-year period (Fig. 1). Platinum ECoG electrode arrays comprised of grids and strips of electrodes were placed subdurally on the brain surface via craniotomy (anatomical locations were clinically determined). Postoperative radiographic imaging was correlated with anatomical brain rendering (Fig. 5). A variety of behavioural tasks were constructed and performed based on the fMRI literature (Table 1). A subset of tasks expected to engage regions incidentally covered by the clinical ECoG array were selected individually for each patient (for example, where the ECoG-covered brain regions would be expected to be active, based on fMRI findings).

Library structure. The library contains a set of zipped folders, with the folder name corresponding to each experiment noted in the left column of Table 1. When unzipped, each folder contains a file titled 'README_[experiment name]_dataset_notes'. Each readme file contains: an ethics statement, including Institutional Review Board (IRB) information, that must be included in the methods section of any publications based on these data; a full reference to the original manuscript(s) where the data were published; the naming conventions for the datafiles and where the files can be found; a description of experimental variables within each datafile; instructions for how to open analysis scripts, initiate analyses and generate figures with analyses plotted on brain surface reconstructions (typically by parsing the commentary of a 'master' script).

The main datafiles are in the 'data' subfolder for each experiment. When applicable, the subfolder 'ref' contains the reference where the experimental data were originally published. Analyses are initiated from the MATLAB scripts contained in each experimental folder—intermediate signal processing results are saved back into the 'data' subfolder and produced figures are saved into the 'figs' subfolder ('figs' is empty until analysis scripts are run). When not in the main datafiles in the 'data' subfolder, patient electrode locations are in subfolders named 'locs' and anatomical reconstructions are in a 'brains' subfolder (if renderings were attainable). If spectral decoupling is performed, a subfolder 'dc_files' is included within the experiment directory ('fixation_PAC', 'fingerflex', 'faces_noise', 'faces_basic'). When a large number of intermediate files are saved and many figures per patient are generated (experiments 'faces_basic',

¹Department of Neurosurgery, Stanford University, Stanford, CA, USA. ²Department of Neurologic Surgery, Mayo Clinic, Rochester, MN, USA.
e-mail: miller.kai@mayo.edu

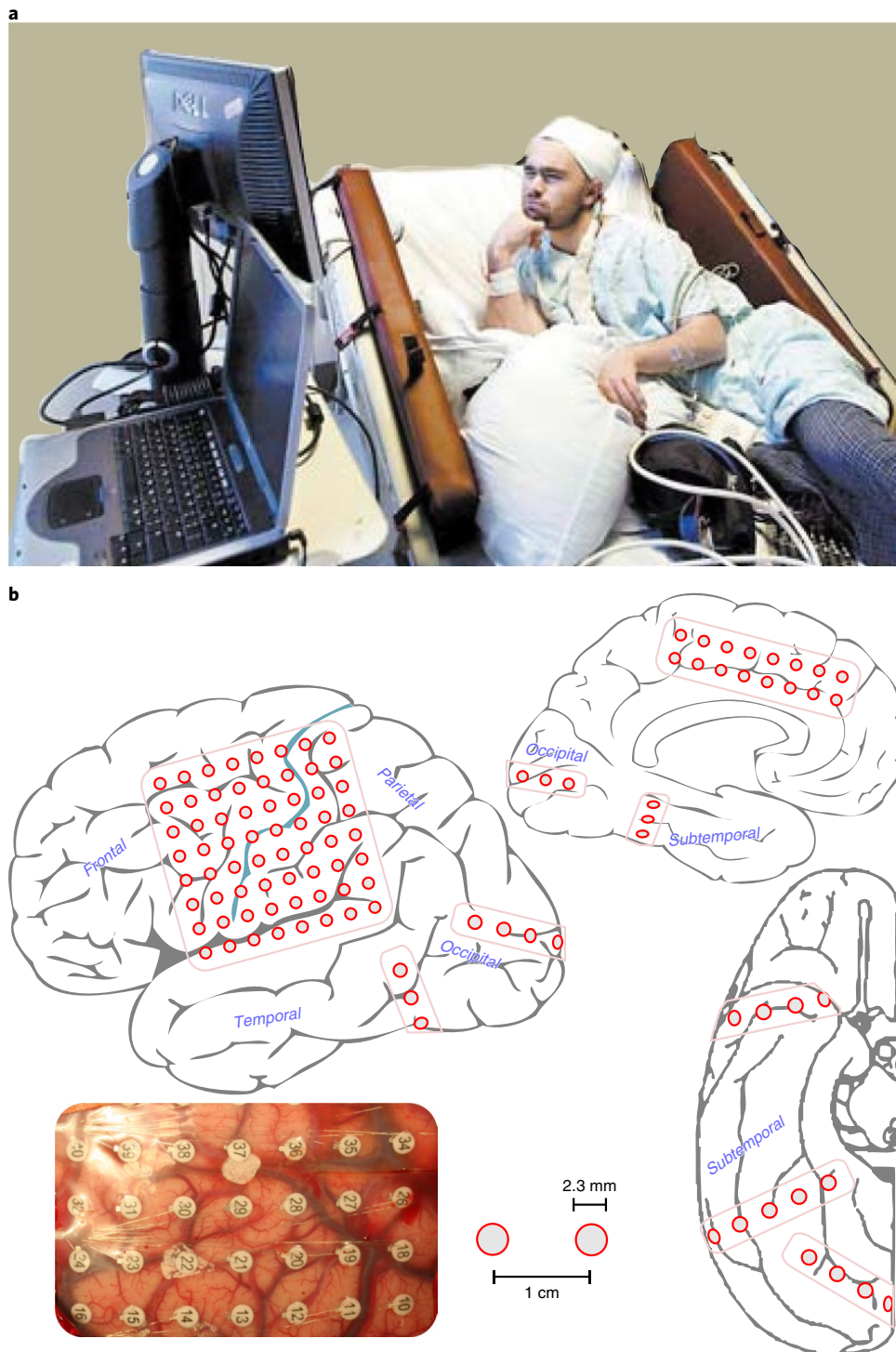


Fig. 1 | Experimental recordings. **a**, Experiments were performed at the bedside, splitting the ECoG signal to separate clinical and research amplifiers. Patients performed behaviours in response to cues from a bedside monitor. **b**, Platinum ECoG electrode arrays were configured as linear strips or grids, embedded in silastic with 1 cm spacing (4 mm diameter with 2.3 mm exposed). They were placed along the subdural space via open craniotomies in the orientations shown. Consent was obtained for use of the non-anonymized image in **a** alongside photographs taken by Jim Bryant for a newspaper article²⁸.

'faces_noise', 'fingerflex', 'fixation_PAC', 'gestures', 'imagery_feedback', 'speech_lists', 'visual_search'), the 'figs' and 'data' subfolders have their own subfolders corresponding to each patient (and named accordingly).

In addition to the experimental folders noted in Table 1, there are four additional folders in the root directory of the library that the experimental folders make use of (these four should be downloaded

and added to the user's MATLAB path): (1) A folder of general MATLAB scripts, used for analyses in many different experiments, titled 'toolbox'. (2) A folder titled 'loc' that contains the scripts for estimating electrode location on the standard Montreal Neurological Institute (MNI) atlas brain (in Talairach coordinates) from X-ray and for plotting results from this localization⁹ (Fig. 5a). (3) A folder titled 'ctmr' contains code for estimating electrode

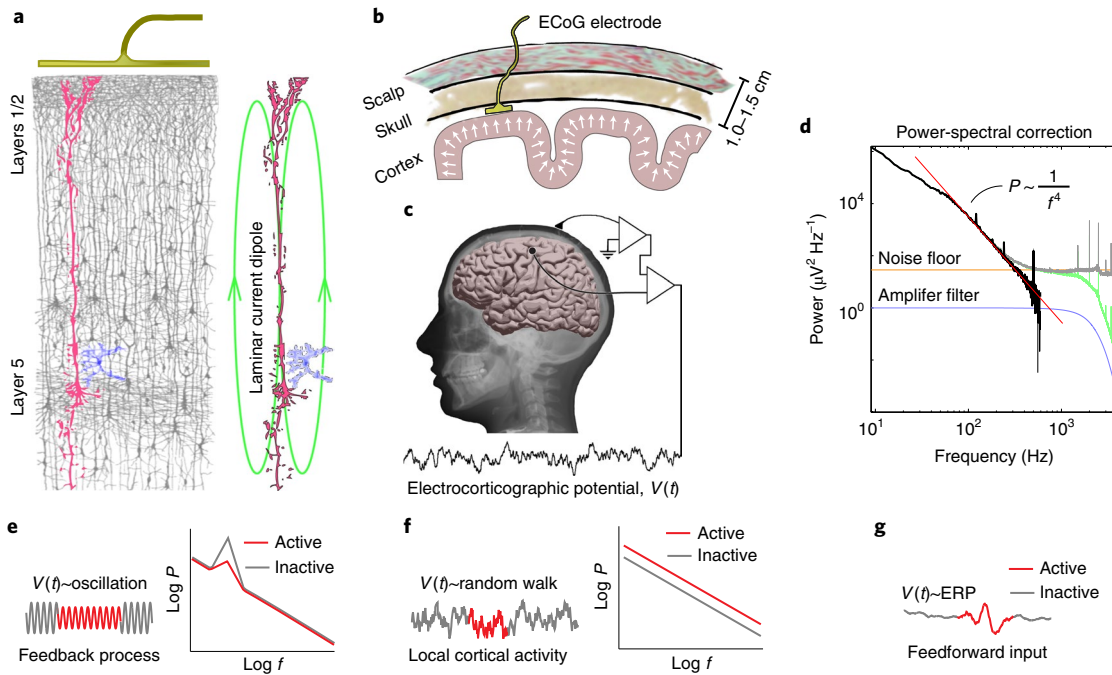


Fig. 2 | The ECoG signal. **a**, The $\sim 5\text{ mm}^2$ of cortical surface beneath each ECoG electrode contains about half a million neurons³⁹, each of which contributes a current dipole produced by charge movement across the cellular membrane⁴⁰. The background is a drawing by Ramon y Cajal of Golgi-stained cortex. **b**, ECoG electrodes are surgically placed subdurally on the cortical surface and are later common average re-referenced after epileptic and artifactual channels are rejected. **c**, ECoG potentials are initially referenced against an external scalp or mastoid reference. **d**, After re-referencing, the ECoG potential PSD can be quantified (green), and then corrected for both the built-in amplifier filter (blue, intermediate PSD in grey) and intrinsic noise floor (orange, final PSD in black). This final PSD is shown to have a power-law shape, tending to $P \sim 1/f^4$ at high frequencies (fit in red, data and analyses from experiment ‘fixation_highfreq’). **e**, Synchronized neural activity in response to feedback loops can be observed in narrow-band oscillations, which are peaks in the PSD. **f**, Aggregate neural activity from a region is revealed by behaviourally associated changes in $1/f$ shape of the PSD⁴. **g**, Synchronized neuronal activity in response to a timed stimulus can be observed in the event-locked averaged raw potential (ERP) and is presumed to be due to feedforward input from a different cortical region. Panels **a–d** are adapted/reproduced from ref. ⁴, PLoS. Panels **e–g** are adapted from the supplement to ref. ¹⁸, PLoS. Credit: Panel **b** was adapted from Ramon y Cajal’s cortex drawings.

positions by fusing pre-operative MRI to postimplant computed tomography (CT)¹⁰ (Fig. 5b). This folder also has many accessory scripts for plotting activity to the patient-specific brain surface rendering (obtained by segmentation of the pre-operative MRI). (4) A folder titled ‘xs_tools’ contains code for estimating and plotting postimplantation CT electrode positions to pre-operative axial MRI slices⁸ (Fig. 5c).

Phenomena observed in ECoG measurements. Extending the work of Crone and colleagues^{11,12}, we found spatially separable motor-associated power changes in ECoG voltage power spectral density (PSD)¹³. At low frequencies (up to $\sim 30\text{ Hz}$), there are spatially broad movement-associated decreases in power in oscillatory processes (brain rhythms) over the peri-central cortical surface. Within the region of low-frequency power change, there are spatially focal, somatotopically discrete, high-frequency (above $\sim 50\text{ Hz}$) power increases (analysis scripts in experiment folder ‘motor_basic’; effect also seen in Fig. 6a).

In order to characterize underlying motifs in the ECoG signal, a technique based on singular-value decomposition was developed for ‘decoupling’ the PSD. This examination revealed broadband power increases that are plainly visible for high frequencies, but are also present in lower frequencies where they are obscured by a simultaneous decrease in power of coincident oscillations^{7,13}. A set of disciplined fitting techniques showed that this broadband process obeys Gaussian statistics, revealed by a power-of-2 structure in the power spectral density (therefore appearing like a random walk in the voltage timeseries), with the form $P \sim 1/f^a$, with P denoting

power and f denoting frequency, such as might be observed in aggregate firing by a population of neurons (Fig. 2a–d,g, fitting techniques implemented in MATLAB scripts gen_10k_spectra.fits.m in experimental folder ‘fixation_highfreq’ and twolorentzfit.m in ‘fixation_pwrlaw’)^{2,4,14}.

An extracted broadband motif from this technique can be applied to a continuous measure of the PSD (the dynamic spectrogram) to track local neuronal activity with high temporal fidelity (Figs. 3c, 4 and 6g)^{3,7} and correlates behaviour with local circuits in a wide variety of settings: early visual cortex while viewing visual stimuli¹⁵ (experiment ‘visual_search’, Fig. 3); ventral temporal category-selective regions while viewing images of faces and other objects^{8,16} (experiments ‘faces_basic’ and ‘faces_noise’, Fig. 4); language and auditory areas during speech¹⁷ (experiments ‘speech_basic’ and ‘speech_lists’); motor regions during hand and finger movements^{7,13,18} (experiments ‘fingerflex’, ‘gestures’, ‘motor_basic’, ‘imagery_basic’, Fig. 6).

In addition to broadband spectral changes, the data also exhibit a diverse set of low-frequency cortical oscillations, revealed by peaks in the PSD (Figs. 2f and 3). In order to understand brain oscillations better, we developed scripts for quantifying single-trial rhythmic entrainment of neuronal activity (‘phase-amplitude coupling’) and calculating single-trial projected coherence between brain sites^{15,18} (Fig. 6; for mathematical descriptions with designation of MATLAB scripts see Methods). Oscillations are found throughout the human cortex, but those within a greek-letter-named frequency range are neither unitary nor ubiquitous and, where observed, are idiosyncratic to specific gyral loci^{18,19}. The greek-letter shorthand should

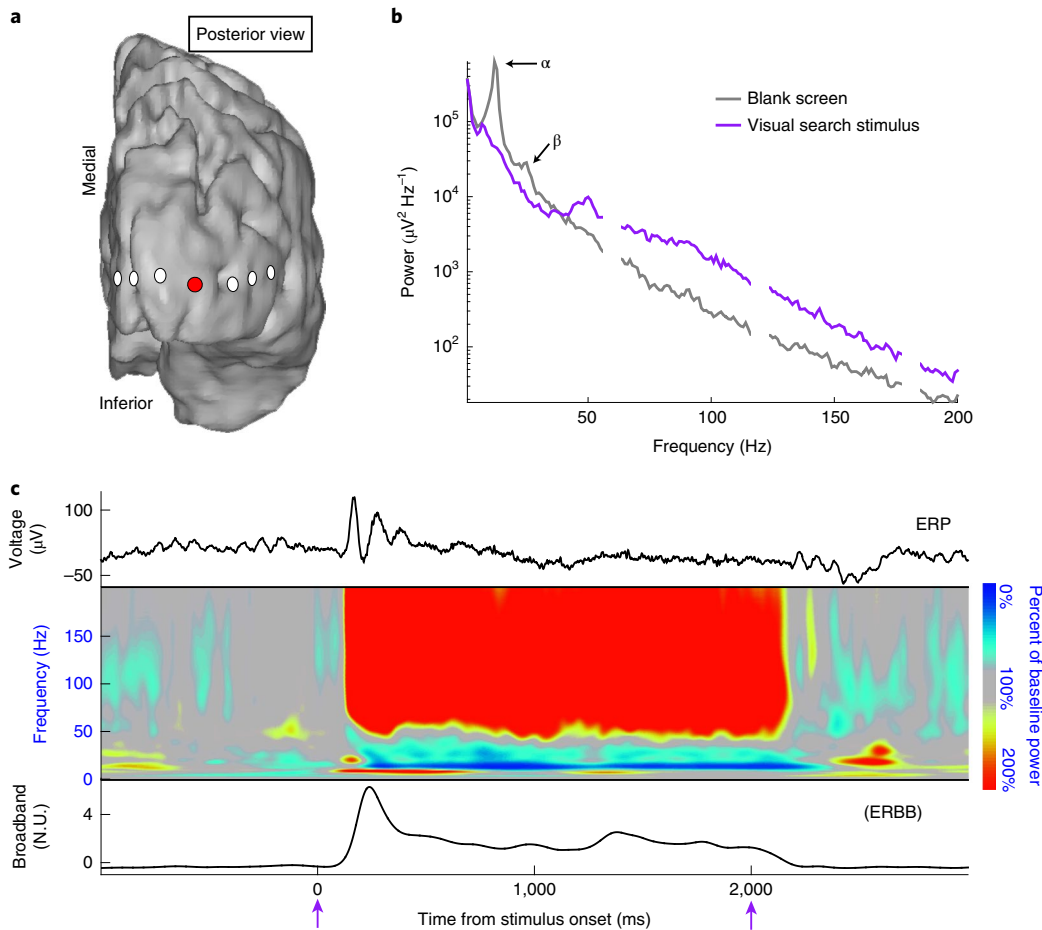


Fig. 3 | An example of basic ECoG changes when a cortical area becomes active. The patient engaged in a simple visual search task for 2 s blocks, interleaved with 2 s blank-screen interstimulus periods (experiment ‘visual_search’). **a**, Position of an occipital pole electrode (red) for which results are shown in **b** and **c**. **b**, Power spectral density during visual search (purple) compared with blank screen (grey). There are prominent oscillations in the ‘alpha’ and ‘beta’ range that are not present during visual search. **c**, Event-averaged changes, from 1 s before each visual search to 1 s after (purple arrows indicate onset and offset of the visual search task). The top trace is the ERP. The fact that there are visually apparent ‘alpha’-oscillations in this trace during blank-screen periods reveals that the stimuli ‘reset’ the ‘alpha’-oscillation (for example, there is a fixed interstimulus interval that does not average away, so its phase must be task-locked). The middle plot is an event-locked averaged spectrogram, showing a power decrease in the ‘alpha’ and ‘beta’ ranges, and broadband increases above that. The bottom broadband trace reveals a sustained event-locked broadband increase throughout the visual search period. Panel **a** adapted from ref.¹⁵, Frontiers Media.

therefore be employed with reservation (here we use quotation marks to emphasize this reservation) and qualified by the brain region where the measurement was made. For example, in our ECoG experiments, we found many topologically specific narrow-band oscillations such as a ~ 10 Hz ‘alpha-rhythm’ on the occipital pole (for example, Fig. 3b; experiment ‘visual_search’), a ~ 16 Hz ‘beta-rhythm’ in the peri-central motor cortex (for example, Fig. 6e; experiment folders ‘motor_basic’, ‘fingerflex’, ‘imagery_feedback’ and ‘gestures’) and a ~ 6 Hz ‘theta-rhythm’ in the lateral frontal convexity (experiment ‘memory_nback’). A few common properties were observed for brain rhythms: first, the amplitude of oscillations decreases at onset of active task engagement (for example, Figs. 3b,c and 6a); second, these decreases are relatively non-specific and completely spatially overlapping for closely related behaviours (for example, different finger movements, Fig. 6); third, oscillations are phase-coherent over several centimetres, along gyrially constrained boundaries (for example, Fig. 6c,d); and fourth, oscillations entrain broadband spectral changes (an analogue of phase-amplitude coupling; for example, Fig. 6e,f)^{13,15,17,18}. Interestingly, the ‘alpha-rhythm’ on the occipital pole is visually apparent in the stimulus-averaged voltage timeseries when images are shown at regular

intervals, suggesting that the phase of alpha-oscillations are reset by the onset and offset of visual stimuli (Fig. 3c; experiment ‘visual_search’)²⁰. Furthermore, this oscillation at stimulus onset appears as a pulsed increase from baseline voltage, rather than a zero-averaged oscillation. This visual observation supports hypotheses that occipital ‘alpha-rhythms’ provide a gating mechanism for information transfer through the occipital cortex via pulsed inhibition^{21,22}. We should note that narrow-band ~ 50 – 70 Hz ‘gamma’ oscillations were not generally observed in our experiments, and recent ECoG work has indicated that these are an idiosyncrasy of visual stimulus properties rather than a necessary property of cortical processing in the occipital lobe²³.

There are evoked changes in the raw voltage trace (event-locked average raw potentials, ERPs) associated with behaviours and sensory stimuli in potentials measured from both the scalp and the brain surface^{24,25}. We found ERPs (Fig. 2g) in the ECoG signal associated with frontal motor cortex electrodes during finger movement (experiment ‘fingerflex’) and in frontal, occipital and temporal cortex while viewing visual stimuli^{15,16,26} (Figs. 3 and 4; experiments ‘visual_search’, ‘memory_nback’, ‘faces_basic’, ‘faces_noise’). While ERPs are found in a wide variety of settings, they are sparse

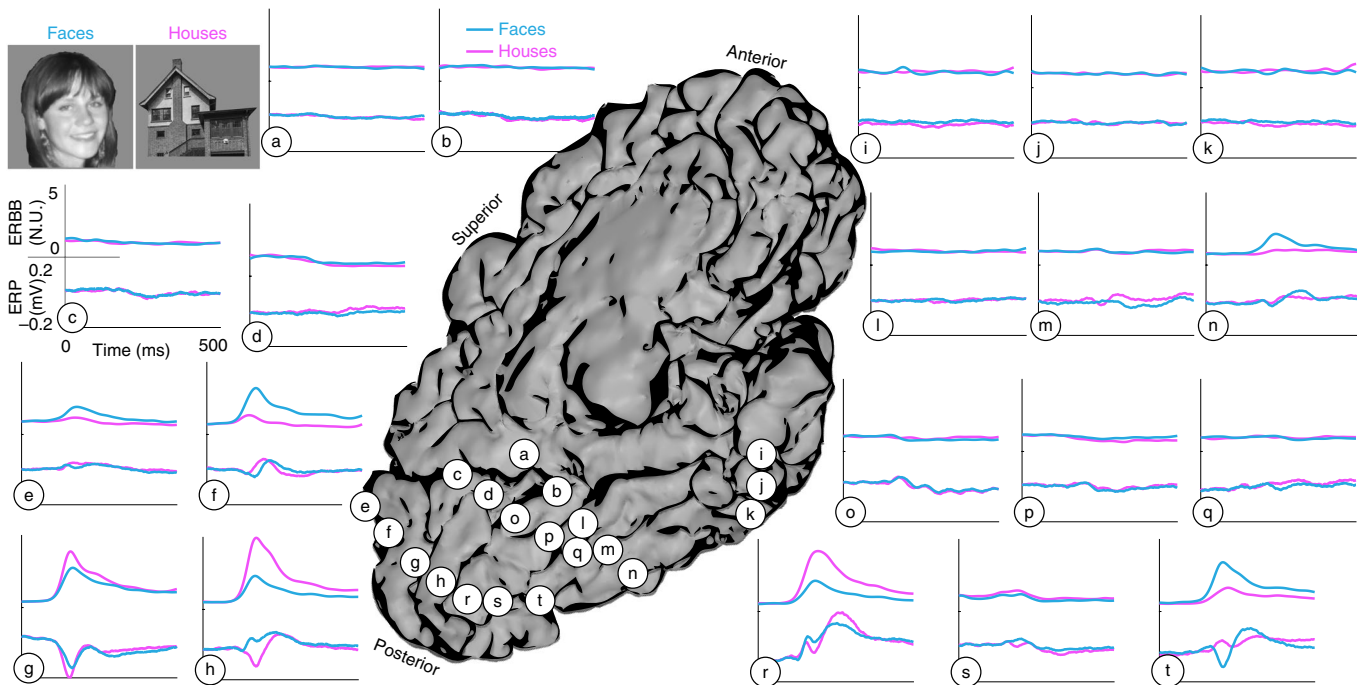


Fig. 4 | Comparison of broadband and ERP changes across the ventral brain surface. During this task, simple face and house pictures (top left) were shown for 400 ms periods, interleaved with 400 ms blank-screen periods. As labelled in **c**, upper traces show event-averaged broadband response (ERBB, measured in normalized units, N.U., representing a z-score of the interstimulus interval) and lower traces show ERP. ECoG ERPs are highly focal. Furthermore, face-selective ERPs are highly polymorphic and there is no simple mapping from broadband selectivity to ERP selectivity²⁶ (experiment ‘faces_basic’). Image adapted from ref. ²⁶, PLoS.

on the brain surface and topologically focal, found only in a few non-contiguous brain sites (Fig. 4). For comparing and contrasting ERP changes with broadband changes in the spontaneous signal, we developed template-projection techniques to quantify and classify behavioural and perceptual states²⁶ (see the MATLAB script flpred_master.m and flpred_classification.m in the ‘faces_basic’ experimental folder) and for designing decoders in control tasks before applying them to a more nuanced, higher-noise, setting¹⁶ (see the MATLAB script fhnoisy_master.m and fhnoisy_classifier.m in the ‘faces_noise’ experimental folder).

Discussion

For new and existing ECoG labs, this library provides a set of basic experiments in a variety of brain areas and behavioural paradigms. To foster discussion about these data, ongoing analyses and resulting publications, we have set up a Facebook group page (‘Kai Miller’s Library of electrocorticography data and analyses’; <https://www.facebook.com/groups/174178755281069/>).

To create a reliable benchmark, we undertook considerable efforts to ensure standardization, relying on one surgeon, one experimenter and one amplifier system with the same settings. For this library, the same surgeon (J. Ojemann) implanted all of the electrodes, to avoid any idiosyncrasies in surgical technique during implantation affecting the character of the recorded signal. Only one experimenter (K.J.M.) interacted with the patients to record all data in this library. The uncontrolled setting of the hospital room can be countered by the regimented practice of the experimenter, and variation among recordings is minimized by ensuring consistency in the experimenter–patient interaction during task instructions. The same set of amplifiers, with the same settings for all experiments, recorded the voltage with reference to a scalp/mastoid electrode (empirically characterized in the supplement to ref. ⁴). It was necessary to split the signal between the research and clinical

amplifiers, but the mechanism used was the same for all recordings. The same brand of electrodes, with the same sizes and composition, was used for all patients. A conjugate approach to the stereotyped benchmark created in this library is to attempt to maximize generalizability by collecting and analysing data across multiple recording sites, with multiple surgeons and multiple experimenters all performing the same set of tasks defined by simple guidelines (one example of which is the ongoing ‘Restoring Active Memory’ project in development²⁷).

For this library, systematic alignment between electrode location and anatomy was contingent on the type and quality of pre- and postimplantation imaging (Fig. 5). In some experiments (‘fixation_’, ‘imagery_’, ‘joystick_track’, ‘mouse_track’ and ‘motor_basic’ folders), only co-registration to a standard atlas, using X-rays, was feasible and scientific claims associated with analysis of these experiments should be limited to general statements about a brain region. For the remainder of experiments, it was possible to fuse pre-implant MRI to postimplant CT (with intraoperative photograph verification), allowing concrete association between physiology and specific gyral anatomy. Electrode locations, along with the necessary plotting tools, are available for every patient in every task and allow for straightforward visualization of overlaid analysed signal properties on brain anatomy.

When assessing data, there are typically multiple ways of approaching a problem and each will have its own intrinsic value. For example: Fourier analysis and Fourier-based wavelets are familiar and help us understand the structure of the data in a language we can relate to (Fig. 3c); conversely, matching pursuit approaches can optimize both how concisely and with what temporal precision the data timeseries is described. The same relationships hold for linear versus nonlinear classification approaches. Often techniques may be mapped onto one another and it can be very useful to examine under what circumstances two complementary

Table 1 | List of experiments

Experiment name	Description	Anatomy	N	Ref(s)
fixation_pwrlaw	The basic baseline fixation task was staring for 2–3 min at an 'X', on the wall 3 m away. Data were examined for power-law structure.	Fronto-parietal-temporal grids	20	4
motor_basic	Simple repetitive movements of the hand (synchronous flexion and extension of all fingers) or tongue (opening of mouth with protrusion and retraction of the tongue: 'sticking the tongue in and out'), at ~1–2 Hz.	Fronto-parietal grids	19	13
fingerflex	Patients were cued with a word displayed on a bedside monitor to move individual fingers repetitively (contralateral to electrode array) during 2 s cue periods while finger position was recorded with a dataglove.	Fronto-parietal grids	9	718
joystick_track	The patient used a joystick to track a counter-clockwise-moving target (hand contralateral to electrode array).	Fronto-parietal grids	4	41
gestures	A series of hand motor tasks involving cued simple individual finger movements, cued gestures or self-generated gestures, while finger position was recorded with a dataglove (hand contralateral to electrode array).	Fronto-parietal grids	5	Data not published
imagery_basic	Patients first performed a cued overt hand and tongue movement task. They subsequently performed a task imagining making identical movements.	Fronto-parietal grids	7	42
imagery_feedback	Patients first performed a cue-based movement task, then a cue-based imagery task, then a one-dimensional cursor control feedback task based on the imagery.	Fronto-parietal grids	4	42
speech_basic	Patients participated in a simple verb-generation task, where nouns were presented on a screen, and the patient would either read the noun or speak a verb that was connected to the noun: for example, if the cue read 'ball', the patient might say 'kick'.	Fronto-parietal-temporal grids	7	17
memory_nback	After a period of baseline fixation, patients performed an <i>n</i> -back working memory task using sequences of house pictures. First they identified when a 'target' house picture appeared (0-back). Second, they identified when a picture had been shown twice in a row (1-back). Finally, they identified when a picture had been repeated with a distracting image in between (2-back).	Right lateral frontal grids	4	Data not published
visual_search	In the visual search task, pictures were shown of arrays of coloured squares. The patient would visually navigate between the squares depending on a cue and report the colour of a targeted square.	Occipital strips, medial and lateral	5	15
faces_basic	Simple face and house pictures were shown in random order for 400 ms each, with 400 ms interstimulus blank screen, and patients reported an upside-down house.	Subtemporal strips	14	826
faces_noise	After performing a simple task viewing face and house pictures, patients then performed a face-detection task using phase-scrambled pictures of faces and houses.	Subtemporal strips	7	16
fixation_PAC	The basic baseline fixation task (as in fixation_pwrlaw) was examined for broadband entrainment on oscillations.	Fronto-parietal-temporal grids	10	18
fixation_highfreq	The basic baseline fixation task (as in fixation_pwrlaw) was performed while recording at 10 kHz. Data were examined for power-law structure.	Fronto-parietal-temporal grids	4	4
mouse_track	Patients used a mouse on a mousepad to track a counter-clockwise moving target (hand contralateral to grid).	Fronto-parietal grids	4	Data not published
speech_lists	These files form a set of speech data for lists of nouns that were first read directly and then used to produce associated action verbs. There were two noun lists, and each list was presented three times for noun reading, then three times for verb production.	Fronto-parietal-temporal grids	4	Data not published

The leftmost column identifies named library folders, downloadable at <https://searchworks.stanford.edu/view/zk881ps0522>. The rightmost column provides the reference in which the relevant experimental data are described. N denotes the number of patients in each experiment.

methods converge. With these library-associated analysis scripts, our published work can be reproduced and methodologies extended to new contexts. As hypotheses emerge in the literature, they can be retested on the library. With the existing analysis

structure, a backbone is in place where data are loaded, variables accessed, figures created and plots cycled through—one may simply insert code at the appropriate place within scripts and have results plotted on anatomy instantly.

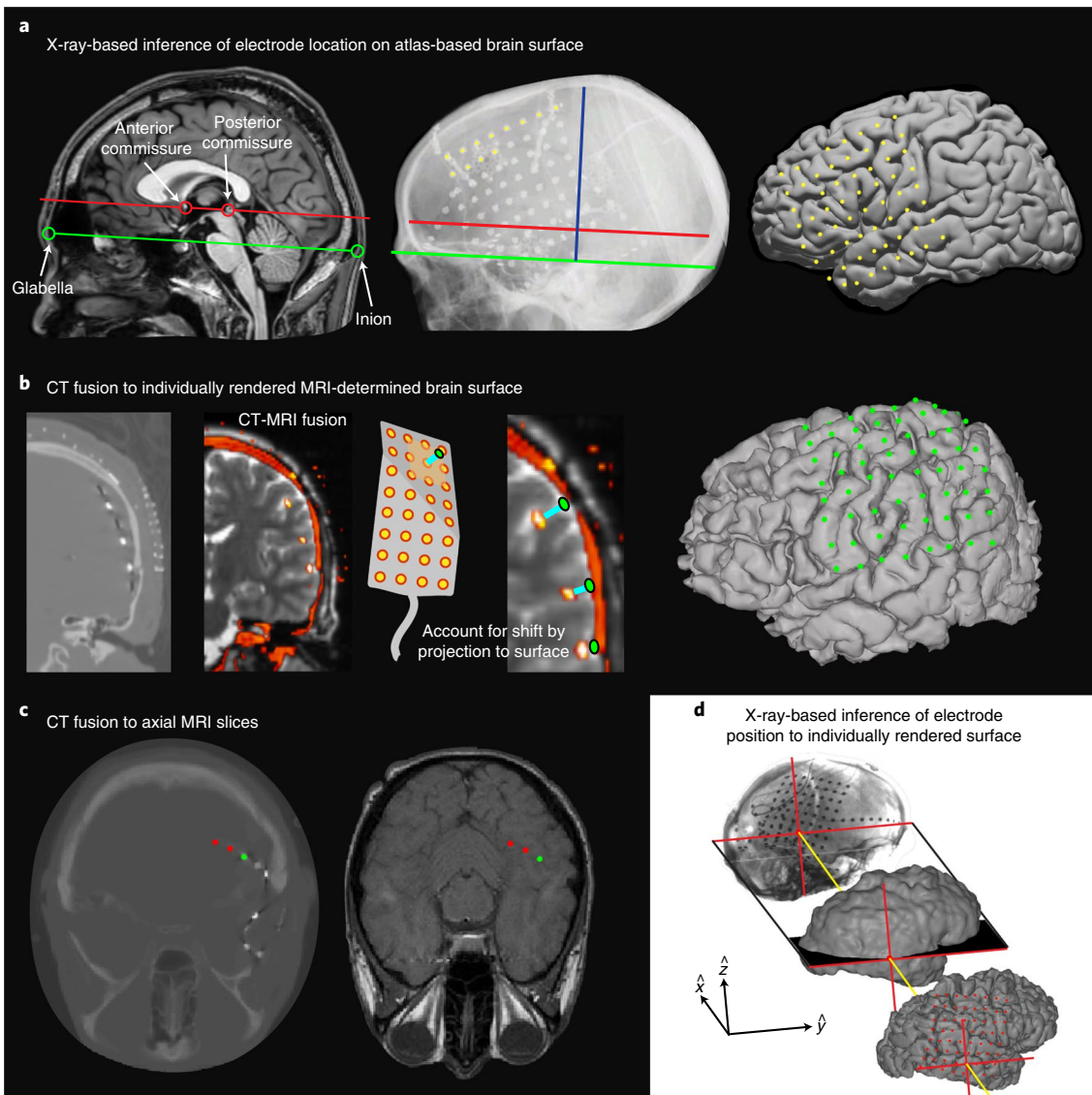


Fig. 5 | Methods for localizing electrode position relative to brain anatomy. **a**, Landmarks on X-ray can be used for localization to an atlas brain rendering, based on the assumption that the anterior commissure–posterior commissure line is parallel to the inio-glabellar line (folder ‘loc’). **b**, The brain surface can be rendered from MRI and fused with postimplantation CT (folder ‘ctmr’). **c**, Electrode locations on CT can be matched to MRI cross section (folder ‘xs_tools’). **d**, Plain film X-ray can be used to estimate electrode position on MRI-based brain surface rendering. Methods are individually described and illustrated in refs. ^{8–10,36}.

Methods

Ethics statement. All 34 patients participated in the experiments in a voluntary manner, after providing informed written consent, under experimental protocols approved by the Institutional Review Board (IRB) of the University of Washington (no. 25203). All patient data were anonymized according to IRB protocol, in accordance with HIPAA mandate. For MRI volumes, each patient’s face was blanked out. The non-anonymized image in Fig. 1a is part of a series taken in anticipation of a newspaper article²⁸, for which the patient provided separate consent. The general convention used for anonymization was to pick the initials of US presidents, with predominantly right/left/both-sided implantations corresponding to Republican/Democrat/other initials, respectively. No link to the patient’s identifying information remains and, as these are anonymized data, no further information about patients will be made available. All data, cortical renderings and analysis code are publicly available, for use without restriction, at <https://searchworks.stanford.edu/view/zk881ps0522>.

Patients. All human subjects in the study were patients with epilepsy at Harborview Hospital in Seattle, WA, USA. Subdural grids and strips of platinum electrodes (Ad-Tech) were clinically placed over frontal, parietal, temporal and occipital cortex for extended clinical monitoring and localization of seizure foci. Placement of electrodes was decided purely based on clinical requirement,

without consideration of possible research involvement. Postoperatively, we examined electrode placement and selected a set of experiments based on the potential for task-responsiveness of the areas covered. A table in the root directory of the library (‘kjm_ECoGLibrary_PatientTaskTable.pdf’) describes which patients performed each task.

Recordings. Experiments were performed at the bedside, using Synamps2 amplifiers (Compumedics Neuroscan) in parallel with clinical recording. Stimuli were presented via a bedside monitor using the general purpose BCI2000 stimulus and acquisition program²⁹ (interacting with proprietary Neuroscan Synamps 2 software), which also recorded behavioural parameters (from dataglove, joystick, audio, EMG, keystroke or mouse) and synchronized them with cortical voltage measurements. Subdural platinum electrode arrays were arranged as combinations of $8 \times [4,6,8]$ rectangular fronto-temporo-parietal arrays and $1 \times [4,6,8]$ linear temporal and occipital strips. The electrodes had 4 mm diameter (2.3 mm exposed), 1 cm interelectrode distance and were embedded in silastic. Neither the composition nor geometry of these electrodes changed during the period in which this library was recorded. Electrical potentials were sampled at 1000 Hz, with respect to a scalp/mastoid reference and ground (not re-referenced, except in the ‘visual_search’ experiment, where it is explicitly stated in the ‘README’ file), with an instrument-imposed bandpass filter from 0.15 to 200 Hz. A preliminary visual examination of

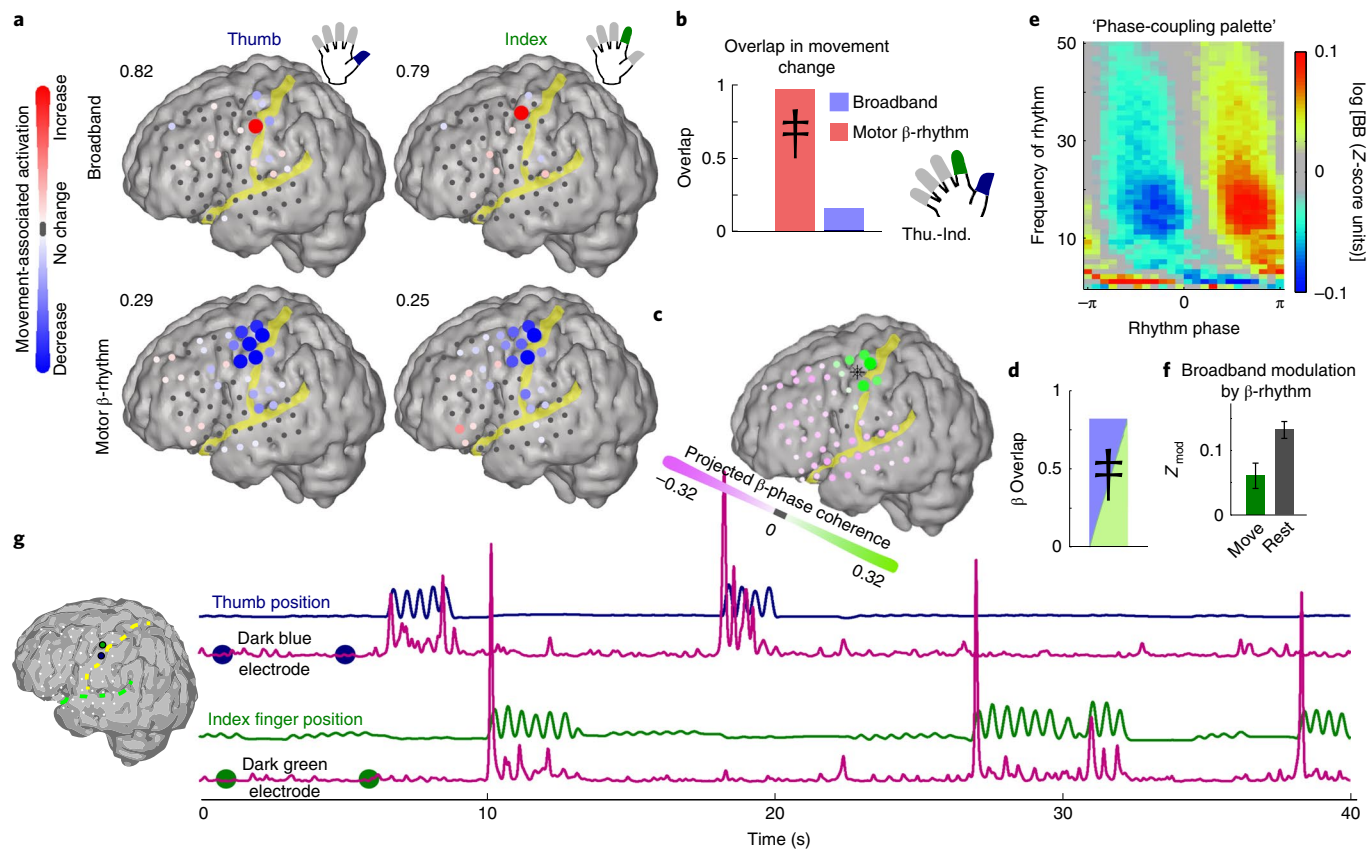


Fig. 6 | Illustrating a range of analyses for a specific setting. A close look into movement-related ECoG changes during a finger movement task. All of the MATLAB scripts and data to perform these analyses are in the experiment ‘fingerflex’. **a**, Changes in broadband and motor ‘beta’-rhythm (12–20 Hz power) at different cortical sites for movement of the thumb and index finger. Colours denote a signed r^2 measurement of increases and decreases in power with movement relative to rest (individually scaled with maximum noted on upper left of each plot). **b**, Quantification of spatial overlap between changes associated with finger movements where 1 is maximum possible overlap and 0 is no overlap. Significance determined by resampling, 10^5 iterations; $\ddagger P < 0.001$ that the overlap happened by chance. **c**, Pairwise complex phase coherence in 12–20 Hz ‘beta’ oscillation signal calculated between the site of greatest broadband change during index finger movement (top right in **a**, designated by a shipwheel symbol) and every other electrode. This complex coherence was then projected onto the phase of the site of maximum absolute phase coherence to obtain the map shown. **d**, Quantification of spatial overlap between projected beta oscillation phase coherence (in **c**) and ‘beta’-rhythm power change associated with index finger movement (bottom right in **a**), significance determined by resampling; $\ddagger P < 0.001$. **e**, log-broadband amplitude (BB) plotted as a function of frequency and phase (‘phase-coupling palette’) for the electrode with the most significant broadband change during thumb movement. **f**, Coupling vector amplitudes (Z_{mod} , mean \pm s.e.m.) for thumb movement (green, $N = 187$) and rest (grey, $N = 1,024$) periods. **g**, Traces of thumb (blue) and index finger (green) position, with corresponding timecourse of broadband spectral change (pink; approximated by the projection of the first PSC to the wavelet-obtained dynamic spectrum) for two cortical sites. Figure partially reproduced from ref. ¹⁸, PLoS.

voltage tracings was performed to reject channels with obvious artefact or epileptic activity (unless explicitly stated otherwise in the ‘README’ file).

Stimulation mapping. For the ‘speech_basic’ experiment, electrocortical stimulation mapping (ECS)^{30,31} was performed to identify the language cortex in the context of clinical care. In this mapping, 5–10 mA square-wave current pulses (1 ms in length) were passed through paired electrodes for up to 3 s (less when a response was evoked) to interrupt function, induce sensation and/or evoke motor responses.

Electrode localization. Throughout the course of our ECoG research, our ability to determine the position of each electrode relative to patient-specific gyral anatomy was variable, and depended on the quality of pre- and postimplantation imaging in each case. Every attempt was made to perform a systematic alignment to anatomy as accurately as possible. In the library, electrode locations, with the necessary plotting tools, are available for every patient and every task.

X-ray landmarks for projection of electrode position to an atlas brain rendering. When only postimplant X-ray (Fig. 5a) or CT scout images were available (for example, when CT and MRI slice thicknesses were too large for volumetric registration), we used a projection technique to estimate the anatomical position of each electrode with respect to a template atlas. For this technique, the line

segment drawn from the glabella to the inion (visible on the lateral X-ray) was estimated as parallel to the anterior commissure–posterior commissure (AC/PC) line, with the actual AC/PC line lying at a fixed ratio of transverse distance to the dorsal aspect of the inner skull table³². By making the assumption that the inner table of the skull matches the brain surface, the maximum antero-posterior (y) and dorsal-ventral (z) coordinates of the inner table of the skull can be normalized to a template brain volume, with identification of a unique medio-lateral (x) coordinate for each y, z along a curved surface that approximates the inner aspect of the dura (a convex hull generated from the cortical surface of the template brain). All electrode positions can be subsequently plotted on the atlas brain to estimate their relationship to underlying anatomy. A MATLAB-based software package (the ‘LOC package’) was constructed to automate this process and allows for easy plotting of data to the atlas brain⁹ (folder ‘loc’ in the root directory of the library).

Projection of postimplantation CT to fully rendered individual patient brain rendering from volumetric MRI. A thin-cut postoperative CT image of the head was fused to a pre-operative structural MRI (Fig. 5b) and the electrode positions determined in the coordinate space of the CT image. A cortical surface mesh was generated from this pre-operative MRI, using either the freesurfer³³ or spm^{34,35} environment. A convex hull generated from the cortical surface and electrodes (often lying below the surface) were projected to this convex hull so that they sit at the cortical surface. This fusion was performed using the CTMR package¹⁰ (folder

'ctmr' in the root directory of the library), which has been demonstrated to localize electrode positions accurately within an error of ~4 mm (the size of the clinical ECoG electrodes).

Reslicing volumetric CT to thick-cut MRI. In some instances (Fig. 5c), we had non-volumetric, thickly cut MRI axial sections, but high-resolution, volumetric, postimplantation CT scans. In this case, the CT was then interpolated and resliced into the T1 axial MRI. Electrodes were then identified in this mutual space on each axial slice so that their positions were known with respect to gyral anatomy from the MRI⁸. A set of simple MATLAB scripts for generating co-registrations and navigating the axial co-registration are in the folder 'xs_files' in the root directory of the library.

X-ray landmarks for projection of electrode position to fully rendered individual brain rendering from volumetric MRI. When high-resolution MRI was available, but only with postimplant X-ray or CT scout images (Fig. 5d), a three-dimensional cortical mesh was obtained using either the freesurfer³³ or spm5 (refs. ^{34,35}) environment. Using a layer-based image-processing program (Photoshop or other), the mesh was rotated into a pure lateral or anterior-posterior view, and then the X-ray manually rotated and scaled so that the brain outline fitted the inner table of the skull. By identifying electrodes on a separate layer from the X-ray, while making the brain-rendering images selectively transparent, electrode positions can be directly visualized at the appropriate points on the brain rendering³⁶.

Tasks. A variety of tasks were performed with each patient, tailored to the approximate functional correlation expected from the functional-imaging literature. Table 1 summarizes these tasks and identifies the appropriate folders in the data library. Within each of these folders is a file named 'README_[folderName]_dataset_notes.pdf' that comprehensively describes:

- The task in detail, with the subfolder locations and naming conventions of datafiles
- Specific descriptions of each variable in the corresponding datasets
- Instructions on the corresponding behavioural recordings (dataglove, joystick, audio, EMG, keystroke, mouse)
- Stimulation results (when applicable), along with file subfolder locations
- Electrode location and brain rendering file subfolder locations

For the tasks with manuscripts published from analyses of the data, the relevant references are included in a 'refs' subfolder.

Methods for signal processing. Note that there are other methods employed in the analyses of many dataset folders and these are described in the manuscripts referenced therein. The corresponding scripts for the finger flexion implementation described below are contained within the 'fingerflex' folder.

Pre-processing. To reduce common artefacts, the raw potential, $V_m^0(t)$, measured at each electrode m was re-referenced with respect to the common average of all M electrodes (script 'car'),

$$V_m(t) = V_m^0(t) - \frac{1}{M} \sum_{i=1}^M V_i^0(t)$$

(channel label, m , henceforth dropped). Electrodes with significant artefact or epileptiform activity were visually rejected before common averaging (as was done for all datasets in the library) and omitted from further analysis.

Power spectral snapshots (script calc_dg_spectra.m in subfolder 'dc_files'). A set of epochs surrounding events τ_q (image presentations or finger movements) were extracted from $V(t)$; each epoch was of duration $T = 1\text{ s}$, $(\tau_q - T/2) < t < (\tau_q + T/2)$. The epochs were sorted according to cue type q and labelled by their event markers τ_q . The power spectral density (PSD) of the epoch flanking time τ_q was calculated as:

$$P(f, q) = \left| \frac{1}{\sqrt{T}} \sum_{t=-T/2}^{+T/2} V(\tau_q + t) H(t) e^{j2\pi ft} \right|^2$$

with f denoting frequency, and Hann windowing function³⁷,

$$H(t) = \frac{1}{2} \left(1 + \cos\left(\frac{2\pi t}{T}\right) \right)$$

Dynamic power spectral measures (script dg_tf_pwr_rm.m in subfolder 'dc_files'). Time-frequency approximations (dynamic spectra) were made using both a wavelet and a Hilbert transform approach (although these can be equivalent under specific conditions, they are used such that they fill different roles and reflect very different quantities in this study).

Wavelet approach. A Morlet wavelet³⁸ of the form

$$\psi(\tau, t) = \exp\left(\frac{i2\pi t}{\tau}\right) \exp\left(\frac{-t^2}{2\tau^2}\right)$$

was multiplied with a sliding window of the voltage timeseries to obtain a time-frequency estimate for every $f = 1/\tau$:

$$\tilde{V}(1/\tau, t) = \sum_{t'=-5\tau/2}^{5\tau/2} V(t+t') \psi(t', \tau)$$

A total of five cycles (5τ) were used to estimate the amplitude and phase of the signal at each frequency for every point in time. In this way, a time-varying Fourier component $\tilde{V}(f, t) = r(f, t) e^{i\phi(f, t)}$ is obtained at each frequency, with fixed uncertainty between the confidence in the estimate of the instantaneous amplitude (r) and phase (ϕ) versus the confidence in temporal resolution.

Event-locked power spectral density. This time-frequency approximation can be used to calculate mean power in relation to the onset of events from each epoch:

$$\bar{P}^V(f, t_w) = \frac{1}{N_v} \sum_{\tau_v} \left(\frac{|\tilde{V}(f, t_w + \tau_v)|^2}{\frac{1}{N_t'} \sum_{t'} |\tilde{V}(f, t')|^2} \right)$$

where τ_v denotes onset times of image presentations or the first finger movement in response to each cue (total N_v) and t' denotes interstimulus times (total N_t'). The peri-image presentation or peri-movement time window of interest is denoted t_w (Fig. 3c).

Hilbert transform approach (script get_rhythm_dist.m). A complex signal to reflect the timecourse of a functionally relevant frequency-range band was constructed as follows: The signal $V(t)$ was band-passed using a third-order Butterworth filter for a specific range, to obtain the 'band-limited' potential, $V(F, t)$, where F denotes the frequency range (for example, for 'beta', $F \rightarrow [12-20\text{ Hz}]$, and so on). A complex, analytic, signal, $\tilde{V}(F, t) = V(F, t) + iV^{IM}(F, t)$ was constructed using the Hilbert transform (for example, such that the new complex signal satisfies the Cauchy-Riemann conditions for analyticity at all times). This signal may also be expressed in polar notation: $\tilde{V}(F, t) = r(F, t) e^{i\phi(F, t)}$. The 'analytic amplitude' of the frequency range F at time t is $r(F, t)$ and the 'phase' is $\phi(F, t)$. The interpretation of ϕ is intuitively difficult, but the most concrete understanding in our context is that the rhythm captured by range F is most surface-positive at $\phi = 0$ and most surface-negative at $\phi = \pi$ or $-\pi$ (this interpretation would not be valid for bipolar re-referenced data). Note that ϕ becomes poorly defined as $r \rightarrow 0$.

Decoupling the cortical spectrum to separate rhythmic activity away from broadband change. The decoupling process is described and illustrated in full detail in the main text and supplement to ref. ⁷.

Principal component decomposition of spectral change (script call_subspc_processing.m, annotated step 5). The samples of the PSD, $P(f, q)$, (total N_q), were first normalized before decomposition.

$$\widehat{P}(f, q) = \ln(P(f, q)) - \ln\left(\frac{1}{N_q} \sum_q P(f, q)\right)$$

A singular-value decomposition then is used to determine the eigenvalues λ_k and eigenvectors \vec{e}_k of the correlation matrix $C(f, f') = \sum_q \widehat{P}(f, q) \widehat{P}(f', q)$, where f and f' are different frequencies.

These eigenvectors, $\vec{C} \vec{e}_k = \lambda_k \vec{e}_k$, the principal spectral components (PSCs), reveal which frequencies vary in power together and are ordered by magnitude of corresponding eigenvalue: $\lambda_1 > \lambda_2 > \dots > \lambda_{N_f}$ where N_f is the number of frequencies and also eigenspectra. If we define the rotation matrix $A(k, f) = (\vec{e}_1, \vec{e}_2, \dots, \vec{e}_{N_f})$, then the projection, $W(k, q)$, of each individual original spectrum in the ensemble onto the new basis vector \vec{e}_k is $W(k, q) = \sum_f A(k, f) \widehat{P}(f, q)$.

The inverse rotation matrix \hat{A}^{-1} , $\hat{A}^{-1} \hat{A} = \hat{I}$, allows us to compare and visualize specific subsets of PSC components with the original full spectrum in frequency space. The second to fourth PSCs typically capture rhythmic power spectral phenomena and power spectra can be reconstructed with and without this rhythmic influence: $\widehat{P}_{\Xi}(f, q) = \sum_{k \in \Xi} A^{-1}(f, k) W(k, q)$.

If the second to fourth PSCs are omitted, $\Xi \rightarrow [1, 5, \dots, N_f]$, then PSDs can be reconstructed where changes in rhythmic spectral phenomena are mostly removed (although there may be residual variance in the decomposition, or some rhythmic influence in all cases). If $\Xi \rightarrow [2-4]$, then PSDs can be reconstructed where changes in rhythmic spectral phenomena are mostly isolated.

The timecourse of broadband spectral change (script `gen_pc_all.m` in subfolder '`dc_files`'). The time-dependent, normalized, dynamic power spectrum, $\widehat{P}(f, q)$, can be obtained in parallel fashion to the spectral snapshots,

$$\widehat{P}(f, t) = \ln(P(f, t)) - \ln\left(\frac{1}{N_t} \sum_t P(f, t)\right)$$

The reflection of the first PSC (\vec{e}_1) in the dynamic spectrum can be estimated by projecting the dynamic spectrum onto it: $\ln A(t) = \sum_f e_1(f) \widehat{P}(f, t)$. We call it $\ln A(t)$ here, because we believe it approximates the logarithm of the timecourse of the coefficient of a power law in the cortical spectrum⁴ of the form $P(f, t) = A(t)f^{-\gamma}$; it is smoothed with a Gaussian window of 50 ms standard deviation, Z-scored and exponentiated to obtain the 'broadband' traces. Because the quantity $\ln A(t)$ is approximately normally distributed, we express it in Z-score units and, for notational brevity, denote it $\chi(t)$ in connection with the broadband power law it reflects. Note that the smoothing and re-exponentiation apply only to the broadband illustrations and not to calculation of coupling to rhythmic phenomena (Fig. 3c).

Broadband coupling to low-frequency phase. The quantification of rhythmic entrainment, phase coherence and spatial overlap, are described and illustrated in full detail in the main text and supplement to ref.¹⁸

Phase-coupling palette (script `gen_pac_matrix_all.m`). The coupling between rhythm phase and local cortical activity is first illustrated by calculating the average log-broadband amplitude $\chi(t)$ as a function of the wavelet-obtained Fourier phase, $\phi(f, t)$, at each Hz. When used to build up a 'palette' displaying many frequencies at once, a full picture of rhythmic entrainment emerges (Fig. 6e).

The coupling vector and trial-by-trial statistics (script `get_rhythm_dist.m`). Because the underlying physiology may have slight cycle-to-cycle variability and non-sinusoidal shape, there may smearing across frequencies in this coupling¹⁹. A rhythm spanning multiple frequencies, F , on the phase-coupling palette can be further characterized by applying a bandpass filter and Hilbert transform to $V(t)$ to obtain the time-dependent Hilbert phase, $\phi(F, t)$. The average log-broadband amplitude $\chi(t)$ as a function of $\phi(F, t)$ in small phase bins, ϕ_k , is denoted χ_k . This allows for the calculation of a 'coupling vector' by taking the dot product $Z_{\text{mod}} e^{i\phi_c} = \frac{1}{2K} \sum_k \chi_k e^{i\phi_k}$. Z_{mod} is the magnitude of coupling between phase of the rhythm, F , and the log-broadband amplitude (because we Z-score $\chi(t)$), Z_{mod} is roughly the amount of variation in the Z-score that can be explained by modulation by the phase of the rhythm concerned) and ϕ_c is the preferred phase of this interaction.

This can be calculated on a trial-by-trial basis, breaking up the data into smaller epochs, n , of continuous movement or rest and calculating a coupling vector for each epoch. Because these individual-epoch $Z_{\text{mod}}(n)$ must be non-negative, the distribution must be significantly greater than zero even when there is no underlying coupling of consistent phase. A true estimate of distributions of coupling should perform a correction that assumes the phase of correction should be reliable.

This is done by projecting each trial's coupling vector onto the preferred phase of the global average coupling vector in the following fashion: first, the global average coupling vector is calculated $\widehat{Z}_{\text{mod}} e^{i\widehat{\phi}_c} = \frac{1}{N} \sum_n Z_{\text{mod}}(n) e^{i\phi_c(n)}$. Note that $\widehat{Z}_{\text{mod}} \neq Z_{\text{mod}}(n)$ and $\widehat{\phi}_c \neq \phi_c(n)$. Second, the individual epoch coupling vectors are projected onto the phase of the average coupling vector to obtain corrected modulation values, $Z_{\text{mod}}^c(n) = Z_{\text{mod}}(n) \cos(\phi_c(n) - \widehat{\phi}_c)$. The quantities $Z_{\text{mod}}^c(n)$ can be negative or positive and can therefore have a distribution significantly overlapping with zero (indicating an absence of reliable coupling). Furthermore, distributions of different types of epochs (for example, visual stimuli, finger movement, rest), each with their own preferred average phase of coupling $\widehat{\phi}_c$, can be compared with one another or with zero (as in Fig. 6f).

Phase coherence of rhythms (script `task_coherencorr.m`). The pairwise phase coherence of an electrode array relative to an internal reference 'seed' site was examined. The complex portion was retained because, in the setting of a dominant distributed rhythm, the choice of a common average reference introduces phase coherence with brain regions where the rhythm is otherwise absent. However, introduced phase coherence will be approximately π radians out of phase with the dominant rhythm. The method to measure phase coherence employed herein reflects only a part of the full phase coherence but is sufficient to address the spatial distribution of pairwise phase coherence. For the complex rhythm $Q_{ab}(F, q) = \frac{1}{T_q} \sum_{t_q} e^{i(\phi_a(F, t_q) - \phi_b(F, t_q))}$ ('seed' electrode a , frequency range $F \rightarrow [12-20\text{Hz}]$), the complex phase coherence with another electrode b , for epoch q (during time t_q) is:

$$Q_{ab}(F, q) = \frac{1}{T_q} \sum_{t_q} e^{i(\phi_a(F, t_q) - \phi_b(F, t_q))}$$

In Fig. 6c, the 'seed' electrode is the motor electrode with the strongest broadband change associated with index finger movement. In order to illustrate the boundaries and dominant motifs in this phase coherence more clearly, the complex phase coherences for all electrodes in an array are projected onto a unit vector in the direction of the phase lag of the site that has the highest absolute phase coherence: if we denote the pairwise complex phase coherence $Q_{ab}(F) = r(a, b) e^{i\phi(a, b)}$ and the phase shift of the pair with maximum phase coherence as ϕ_{\max} then the projected phase coherence is $Q_{ab}^c(F) = r(a, b) \cos(\phi(a, b) - \phi_{\max})$ (Fig. 6c, shipwheel symbol denotes seed site).

Quantifying overlap in spatial distribution (script `coh_overlap_work.m`). In order to quantify the overlap between spatial extent and degree of change in two different measures, we use a resampling metric. For measures of types X_m and Y_m (m denoting electrode), the simple dot product between the two gives a 'true' overlap, $O_{XY}^T = \sum_m X_m Y_m$ that can be compared to surrogate distributions for quantification of magnitude and significance. The spatial overlap metric is the true overlap divided by the maximum possible overlap if electrode labels were reassigned: Overlap = $\frac{O_{XY}^T}{\sum_m X'_m Y'_m}$ where X'_m , Y'_m denote the distributions X_m , Y_m re-sorted in ascending order. To estimate the significance of this overlap using resampling, the electrode labels are then randomly scrambled ($m \rightarrow l$) and at the k th surrogate overlap is obtained: $O_{XY}^S(k) = \sum_l X_l Y_l$. This is done 10^6 times. A p-value for the significance of the overlap is the percentage of O_{XY}^S that are greater than O_{XY}^T (or the percentage that are less in the case that $O_{XY}^T < 0$, Fig. 6b,d).

Reporting Summary. Further information on research design is available in the Nature Research Reporting Summary linked to this article.

Received: 9 September 2018; Accepted: 5 July 2019;

Published online: 26 August 2019

References

- Katzner, S. et al. Local origin of field potentials in visual cortex. *Neuron* **61**, 35–41 (2009).
- Miller, K. J. Broadband spectral change: evidence for a macroscale correlate of population firing rate? *J. Neurosci.* **30**, 6477 (2010).
- Miller, K. J. et al. Broadband changes in the cortical surface potential track activation of functionally diverse neuronal populations. *Neuroimage* **85**(Pt 2), 711–720 (2014).
- Miller, K. J., Sorensen, L. B., Ojemann, J. G. & den Nijs, M. Power-law scaling in the brain surface electric potential. *PLoS Comput. Biol.* **5**, e1000609 (2009).
- Manning, J. R., Jacobs, J., Fried, I. & Kahana, M. J. Broadband shifts in LFP power spectra are correlated with single-neuron spiking in humans. *J. Neurosci.* **29**, 13613–13620 (2009).
- Gazzaniga, M. S. *The Cognitive Neurosciences* (MIT Press, 2009).
- Miller, K. J., Zanos, S., Fetz, E. E., den Nijs, M. & Ojemann, J. G. Decoupling the cortical power spectrum reveals real-time representation of individual finger movements in humans. *J. Neurosci.* **29**, 3132 (2009).
- Miller, K. J., Hermes, D., Witthoft, N., Rao, R. P. & Ojemann, J. G. The physiology of perception in human temporal lobe is specialized for contextual novelty. *J. Neurophysiol.* **114**, 256–263 (2015).
- Miller, K. J., Makeig, S., Hebb, A. O., Rao, R. P. & Ojemann, J. G. Cortical electrode localization from X-rays and simple mapping for electrocorticographic research: The "Location on Cortex" (LOC) package for MATLAB. *J. Neurosci. Methods* **162**, 303–308 (2007).
- Hermes, D., Miller, K. J., Noordmans, H. J., Vansteensel, M. J. & Ramsey, N. F. Automated electrocorticographic electrode localization on individually rendered brain surfaces. *J. Neurosci. Methods* **185**, 293–298 (2010).
- Crone, N. E. et al. Functional mapping of human sensorimotor cortex with electrocorticographic spectral analysis. I. Alpha and beta event-related desynchronization. *Brain* **121**, 2271–2299 (1998).
- Crone, N. E., Miglioretti, D. L., Gordon, B. & Lesser, R. P. Functional mapping of human sensorimotor cortex with electrocorticographic spectral analysis. II. Event-related synchronization in the gamma band. *Brain* **121**, 2301–2315 (1998).
- Miller, K. J. et al. Spectral changes in cortical surface potentials during motor movement. *J. Neurosci.* **27**, 2424–2432 (2007).
- Miller, K. J., Sorensen, L. B., Ojemann, J. G. & den Nijs, M. D. ECoG observations of power-law scaling in the human cortex. Preprint at arXiv <https://arxiv.org/abs/0712.0846v1> (2007).
- Miller, K. J. et al. Dynamic modulation of local population activity by rhythm phase in human occipital cortex during a visual search task. *Front Hum. Neurosci.* **4**, 197 (2010).
- Miller, K. J., Hermes, D., Pestilli, F., Wig, G. S. & Ojemann, J. G. Face percept formation in human ventral temporal cortex. *J. Neurophysiol.* **118**, 2614–2627 (2017).
- Miller, K. J., Abel, T. J., Hebb, A. O. & Ojemann, J. G. Rapid online language mapping with electrocorticography. *J. Neurosurg. Pediatr.* **7**, 482–490 (2011).

18. Miller, K. J. et al. Human motor cortical activity is selectively phase-entrained on underlying rhythms. *PLoS Comput. Biol.* **8**, e1002655 (2012).
19. Hermes, D. et al. Cortical theta wanes for language. *Neuroimage* **85**, 738–748 (2014).
20. Hanslmayr, S. et al. Alpha phase reset contributes to the generation of ERPs. *Cereb. Cortex* **17**, 1–8 (2006).
21. Schalk, G. A general framework for dynamic cortical function: the function-through-biased-oscillations (FBO) hypothesis. *Front. Hum. Neurosci.* **9**, 352 (2015).
22. Jensen, O. & Mazaheri, A. Shaping functional architecture by oscillatory alpha activity: gating by inhibition. *Front. Hum. Neurosci.* **4**, 186 (2010).
23. Hermes, D., Miller, K., Wandell, B. & Winawer, J. Stimulus dependence of gamma oscillations in human visual cortex. *Cereb. Cortex* **25**, 2951–2959 (2014).
24. Davis, P. A. Effects of acoustic stimuli on the waking human brain. *J. Neurophysiol.* **2**, 494–499 (1939).
25. Jasper, H. & Penfield, W. Electrocorticograms in man: effect of voluntary movement upon the electrical activity of the precentral gyrus. *Arch. f. Psychiatri. und Nervenkrankh.* **183**, 163–174 (1949).
26. Miller, K. J., Schalk, G., Hermes, D., Ojemann, J. G. & Rao, R. P. Spontaneous decoding of the timing and content of human object perception from cortical surface recordings reveals complementary information in the event-related potential and broadband spectral change. *PLoS Comput. Biol.* **12**, e1004660 (2016).
27. University of Pennsylvania. Restoring Active Memory (RAM) <http://memory.psych.upenn.edu/RAM> (2018).
28. Paulson, T. Thought powers computer, *Seattle Post-Intelligencer* (16 December 2004).
29. Schalk, G., McFarland, D. J., Hinterberger, T., Birbaumer, N. & Wolpaw, J. R. BCI2000: a general-purpose brain-computer interface (BCI) system. *IEEE Trans. Biomed. Eng.* **51**, 1034–1043 (2004).
30. Ojemann, G., Ojemann, J., Lettich, E. & Berger, M. Cortical language localization in left, dominant hemisphere. An electrical stimulation mapping investigation in 117 patients. *J. Neurosurg.* **71**, 316 (1989).
31. Ojemann, G. A. Models of the brain organization for higher integrative functions derived with electrical stimulation techniques. *Hum. Neurobiol.* **1**, 243 (1982).
32. Fox, P. T., Perlmuter, J. S. & Raichle, M. E. A stereotactic method of anatomical localization for positron emission tomography. *J. Comput. Assist. Tomogr.* **9**, 141–153 (1985).
33. Dale, A. M., Fischl, B. & Sereno, M. I. Cortical surface-based analysis. I. Segmentation and surface reconstruction. *Neuroimage* **9**, 179–194 (1999).
34. Ashburner, J. & Friston, K. J. Unified segmentation. *Neuroimage* **26**, 839–851 (2005).
35. Friston, K. J. et al. Statistical parametric maps in functional imaging: a general linear approach. *Hum. Brain Mapp.* **2**, 189–210 (1995).
36. Miller, K. J. et al. Brain surface electrode co-registration using MRI and X-ray. *Engineering in Medicine and Biology Society (EMBC), 2010 Annual International Conference of the IEEE* 6015–6018 (IEEE, 2010).
37. Porat, B. *A Course in Digital Signal Processing* (Wiley, 1997).
38. Goupiaud, P., Grossmann, A. & Morlet, J. Cycle-octave and related transforms in seismic signal analysis. *Geoexploration* **23**, 85–102 (1984).
39. Pakkenberg, B. & Gundersen, H. J. G. Neocortical neuron number in humans: effect of sex and age. *J. Comp. Neurol.* **384**, 312–320 (1997).
40. Mitzdorf, U. Current source-density method and application in cat cerebral cortex: investigation of evoked potentials and EEG phenomena. *Physiol. Rev.* **65**, 37–100 (1985).
41. Schalk, G. et al. Two-dimensional movement control using electrocorticographic signals in humans. *J. Neural Eng.* **5**, 75–84 (2008).
42. Miller, K. J. et al. Cortical activity during motor execution, motor imagery, and imagery-based online feedback. *Proc. Natl Acad. Sci. USA* **108**, 4430–4435 (2010).

Acknowledgements

I am grateful to J. Ojemann, M. den Nijs, R. Rao and G. Schalk for many years of selfless mentorship during the development of this library. D. Hermes, R. Eisinger and B. Wandell provided many helpful discussions about open data and helped with critical readings of this manuscript. The scientific value of the time spent by our patients at Harborview Hospital in Seattle is immense and I am thankful for their enthusiastic participation. I am financially supported by the Van Wagenen Foundation. Data collection was supported by NSF grant no. BCS-0642848 and NIH grant no. RO1NS065186. The funders had no role in study design, data collection and analysis, decision to publish or preparation of the manuscript.

Competing interests

The author has no competing interests.

Additional information

Supplementary information is available for this paper at <https://doi.org/10.1038/s41562-019-0678-3>.

Reprints and permissions information is available at www.nature.com/reprints.

Correspondence and requests for materials should be addressed to K.J.M.

Peer review information: Primary Handling Editor: Marike Schiffer.

© The Author(s), under exclusive licence to Springer Nature Limited 2019

Reporting Summary

Nature Research wishes to improve the reproducibility of the work that we publish. This form provides structure for consistency and transparency in reporting. For further information on Nature Research policies, see [Authors & Referees](#) and the [Editorial Policy Checklist](#).

Statistical parameters

When statistical analyses are reported, confirm that the following items are present in the relevant location (e.g. figure legend, table legend, main text, or Methods section).

n/a Confirmed

- The exact sample size (n) for each experimental group/condition, given as a discrete number and unit of measurement
- An indication of whether measurements were taken from distinct samples or whether the same sample was measured repeatedly
- The statistical test(s) used AND whether they are one- or two-sided
Only common tests should be described solely by name; describe more complex techniques in the Methods section.
- A description of all covariates tested
- A description of any assumptions or corrections, such as tests of normality and adjustment for multiple comparisons
- A full description of the statistics including central tendency (e.g. means) or other basic estimates (e.g. regression coefficient) AND variation (e.g. standard deviation) or associated estimates of uncertainty (e.g. confidence intervals)
- For null hypothesis testing, the test statistic (e.g. F , t , r) with confidence intervals, effect sizes, degrees of freedom and P value noted
Give P values as exact values whenever suitable.
- For Bayesian analysis, information on the choice of priors and Markov chain Monte Carlo settings
- For hierarchical and complex designs, identification of the appropriate level for tests and full reporting of outcomes
- Estimates of effect sizes (e.g. Cohen's d , Pearson's r), indicating how they were calculated
- Clearly defined error bars
State explicitly what error bars represent (e.g. SD, SE, CI)

Our web collection on [statistics for biologists](#) may be useful.

Software and code

Policy information about [availability of computer code](#)

Data collection

BCI2000; Neuroscan

Data analysis

MATLAB; Freesurfer; SPM08

For manuscripts utilizing custom algorithms or software that are central to the research but not yet described in published literature, software must be made available to editors/reviewers upon request. We strongly encourage code deposition in a community repository (e.g. GitHub). See the Nature Research [guidelines for submitting code & software](#) for further information.

Data

Policy information about [availability of data](#)

All manuscripts must include a [data availability statement](#). This statement should provide the following information, where applicable:

- Accession codes, unique identifiers, or web links for publicly available datasets
- A list of figures that have associated raw data
- A description of any restrictions on data availability

All data and code are fully available, for use without restriction (other than attribution) at: <https://searchworks.stanford.edu/view/zk881ps0522>

Field-specific reporting

Please select the best fit for your research. If you are not sure, read the appropriate sections before making your selection.

Life sciences Behavioural & social sciences Ecological, evolutionary & environmental sciences

For a reference copy of the document with all sections, see nature.com/authors/policies/ReportingSummary-flat.pdf

Life sciences study design

All studies must disclose on these points even when the disclosure is negative.

Sample size	not relevant
Data exclusions	portions data that were determined to have significant artifact or to be epileptic were excluded.
Replication	all data and the methods for analyzing these data are fully available online at: https://searchworks.stanford.edu/view/zk881ps0522
Randomization	not relevant
Blinding	not relevant

Reporting for specific materials, systems and methods

Materials & experimental systems

n/a	Involved in the study
<input checked="" type="checkbox"/>	<input type="checkbox"/> Unique biological materials
<input checked="" type="checkbox"/>	<input type="checkbox"/> Antibodies
<input checked="" type="checkbox"/>	<input type="checkbox"/> Eukaryotic cell lines
<input checked="" type="checkbox"/>	<input type="checkbox"/> Palaeontology
<input checked="" type="checkbox"/>	<input type="checkbox"/> Animals and other organisms
<input checked="" type="checkbox"/>	<input checked="" type="checkbox"/> Human research participants

Methods

n/a	Involved in the study
<input checked="" type="checkbox"/>	<input type="checkbox"/> ChIP-seq
<input checked="" type="checkbox"/>	<input type="checkbox"/> Flow cytometry
<input checked="" type="checkbox"/>	<input type="checkbox"/> MRI-based neuroimaging

Human research participants

Policy information about [studies involving human research participants](#)

Population characteristics epileptic patients who were undergoing surgical implantation for seizure monitoring participated under an IRB approved protocol.

Recruitment Epileptic patients who were undergoing surgical implantation for seizure monitoring were approached by non-clinical staff about the possibility of volunteering to participate. all research was performed on a fully-revocable volunteer basis, completely separate from their care, with no added risk to them in any way in the event that they participated (or did not participate in research). If they chose not to participate, there was no effect on their care whatsoever. they were free to stop behavioral tasks at any point.